nature physics

LETTERS

https://doi.org/10.1038/s41567-017-0031-6

Superconductivity in few-layer stanene

Menghan Liao[1], Yunyi Zang[1], Zhaoyong Guan[1], Haiwei Li[1], Yan Gong[1], Kejing Zhu[1], Xiao-Peng Hu[1,2], Ding Zhang[1,2]*, Yong Xu[1,2,3]*, Ya-Yu Wang[1,2], Ke He[1,2], Xu-Cun Ma[1,2], Shou-Cheng Zhang[4] and Qi-Kun Xue[1,2]*

A single atomic slice of α-tin—stanene—has been predicted to host the quantum spin Hall effect at room temperature, offering an ideal platform to study low-dimensional and topological physics. Although recent research has focused on monolayer stanene, the quantum size effect in few-layer stanene could profoundly change material properties, but remains unexplored. By exploring the layer degree of freedom, we discover superconductivity in few-layer stanene down to a bilayer grown on PbTe, while bulk α-tin is not superconductive. Through substrate engineering, we further realize a transition from a single-band to a two-band superconductor with a doubling of the transition temperature. In situ angle-resolved photoemission spectroscopy (ARPES) together with first-principles calculations elucidate the corresponding band structure. The theory also indicates the existence of a topologically non-trivial band. Our experimental findings open up novel strategies for constructing two-dimensional topological superconductors.

Confining superconductivity to a two-dimensional (2D) plane engenders a variety of quantum phenomena[1,2]. Of late, the realization of highly crystalline and atomically thin superconductors has triggered a flurry of discoveries, including the Griffiths singularity behavior[3] and a quantum metallic phase[4,5], as well as an extremely large critical magnetic field in the plane[6,7]. One strategy for achieving 2D superconductors is to epitaxially grow superconductive single elements, such as Pb, In and Ga, for just one or two atomic layers[3,8,9]. Among the single elements, tin (Sn) is the very material in which the Meissner effect was first discovered[10], but realizing ultrathin Sn in the superconductive β-phase, known as white tin[11], remains challenging. The epitaxially grown Sn in the ultrathin limit tends to fall instead in the α-phase[12], whose bulk is semi-metallic and non-superconductive.

Recently, however, intensive research has been devoted to investigate the thinnest possible slice of α-tin(111)—a counterpart of graphene called stanene[13]. Stanene promises various exotic features, such as highly efficient thermoelectrics[14], topological superconductivity[15], and high-temperature quantum spin Hall[16] and quantum anomalous Hall effects[17]. Monolayer stanene that has been successfully fabricated by molecular beam epitaxy on Bi_2Te_3(111) (ref. [18]) and PbTe(111) (ref. [19]) is the focus of current research. On the other hand, few-layer stanene is expected to show significant thickness-dependent properties due to the strong quantum confinement[20], but its exploration is still lacking.

In this Letter, by going from monolayer to few-layer stanene, surprisingly, we discover superconductivity. We report the stable superconducting properties of uncapped few-layer stanene films on PbTe (111)/Bi_2Te_3 substrates. The superconducting transition temperature (T_c) can be effectively enhanced by varying the thickness of the PbTe buffer layer. Concomitantly with a doubling of T_c, we observe a single-band to two-band transition, which is further elucidated by photoemission spectroscopy and theoretical calculations. The calculated band structure further indicates the existence of inverted bands in our system. Our results therefore underscore the potential of an in-plane integration of 2Dtopological insulator and superconductor—of the same material. The heterostructure, vertically consisting of superconducting few-layer stanene and topological insulator Bi_2Te_3, may also be of interest for inducing topological superconductivity via the proximity effect[21].

Figure 1a schematically illustrates the sandwich structure of our system with a trilayer Sn on top of PbTe/Bi_2Te_3/Si(111). The α-phase of Sn is confirmed by in situ structural analysis (see Extended Data Figure 1). The dangling bonds on the top surface (Fig. 1a) are presumably saturated, which is evidenced by our ARPES data showing large band gaps at the K/K′ points[18,19]. The saturation might be caused by hydrogen, a ubiquitous residue in the crystal growth environment[22], resulting in chemically stable samples. Figure 1b shows that superconductivity emerges starting from a bilayer. By increasing the number of Sn layers (N_{Sn}), the transition temperature is consecutively promoted. In general, T_c scales with $1/N_{Sn}$ (Fig. 1d), as has been seen previously in other ultrathin films[1,2]. We confirm the Meissner effect by a two-coil mutual inductance technique in Extended Data Figure 2. Extended Data Figure 3 further reveals the 2D nature of such a superconductor, evidenced by anisotropic critical magnetic fields and the Berezinskii–Kosterlitz–Thouless transition. As shown in Fig. 1c, superconductivity also depends keenly on the thickness of the PbTe layer (N_{PbTe}). It emerges at $N_{PbTe}=6$, and T_c further doubles when N_{PbTe} exceeds 8. We speculate that this evolution stems from the change in density of states as well as the release of strain from the lattice mismatch (see Methods)[19]. A thicker PbTe might host more surface vacancies due to the lowered formation energy[23,24], thus providing more electron doping into Sn, as we will reveal by ARPES later. Notably, the superconductivity in these uncapped samples barely changes after exposure to air, as exemplified by the data taken in the second cool-down after more than two weeks of storage (Fig. 1c). Extended Data Figure 2 further documents the superconductivity after one year of storage. In contrast, previous ex situ transport studies on ultrathin Pb, In, and Ga films all rely on capping with an additional layer of Au or Ag[1–3]. We also show traces from two pairs of samples with the same nominal thicknesses, attesting to precise growth control. The transition temperature T_c as a function

[1]State Key Laboratory of Low-Dimensional Quantum Physics, Department of Physics, Tsinghua University, Beijing, China. [2]Collaborative Innovation Center of Quantum Matter, Beijing, China. [3]RIKEN Center for Emergent Matter Science (CEMS), Wako, Saitama, Japan. [4]Department of Physics, McCullough Building, Stanford University, Stanford, CA, USA. Menghan Liao and Yunyi Zang contributed equally to this work. *e-mail: dingzhang@mail.tsinghua.edu.cn; yongxu@mail.tsinghua.edu.cn; qkxue@mail.tsinghua.edu.cn

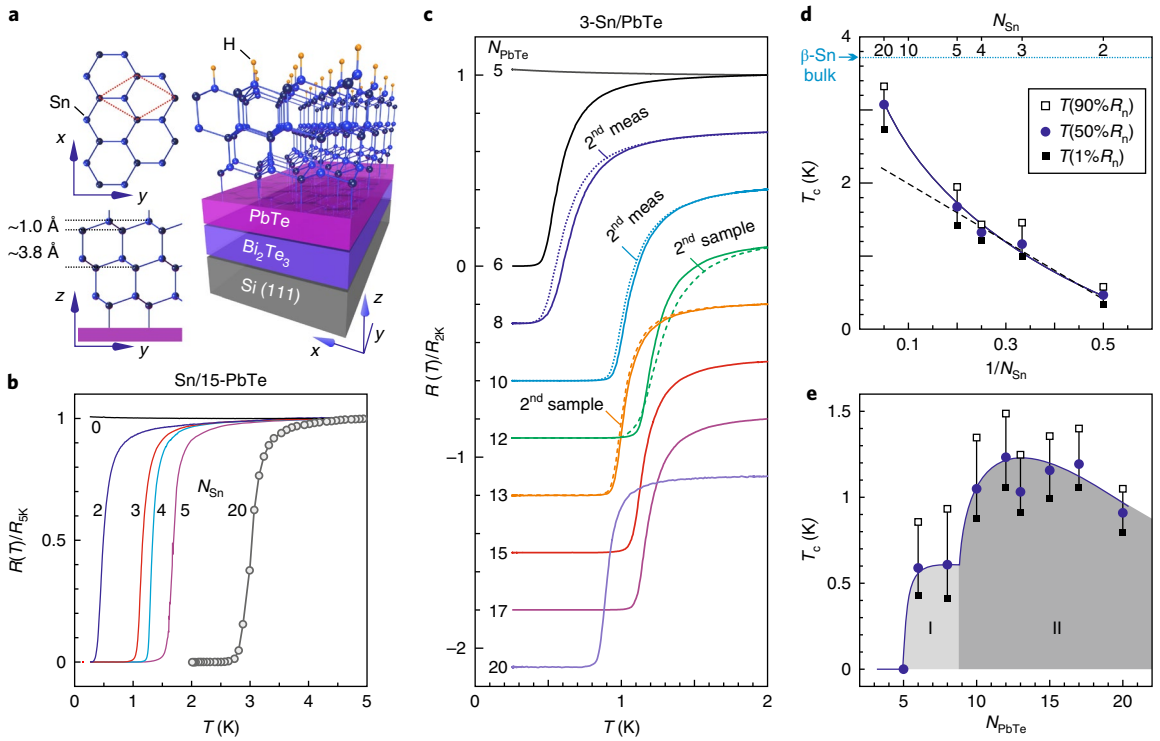

Fig. 1 | Superconductive properties of few-layer stanene. a, Illustration of stanene lattice and Sn/PbTe/Bi_2Te_3 sandwich structure. The upper left panel shows a top view of only one layer of stanene. Distances marked are from first-principles calculations. **b**, Normalized resistance of stanene with increasing number of layers grown on substrates consisting of 15-PbTe/5-Bi_2Te_3/Si(111). **c**, Normalized resistance of trilayer stanene (3-Sn) grown on different thicknesses of PbTe substrates. Numbers in the panel indicate the number of PbTe layers. Dotted curves represent the data from the second measurement after 15–20 days of storage in a glovebox. Dashed curves are from a second sample grown with the same nominal thickness. Except for the top two, the curves are equally offset for clarity. **d**,**e**, Critical temperature (T_c) as a function of the number of stanene layers (**d**) or PbTe layers (**e**). The three data points of T_c in a row represent the temperatures where the resistance drops to 1%, 50% and 90% of the normal resistance (R_n), respectively. The dashed straight line and solid curves in **d** and **e** are guides for the eye. For $N_{Sn}=20$, the superconducting transition temperature approaches that of bulk β-Sn: 3.7 K (ref. [11]).

of N_{PbTe} is given in Fig. 1e. The shaded regions represent two regimes corresponding to samples with $T_c \sim 0.5$ K and those with $T_c \sim 1.2$ K.

Transport properties of trilayer stanene in regimes I and II are distinctly different. For 3-Sn/10-PbTe in regime II, the critical current displays two steps with increasing temperature, with a kink at about 0.5 K (Fig. 2a)—a characteristic feature of two-band superconductivity[25]. This two-band nature is further confirmed by the temperature dependence of the upper critical field[26,27]. The 3-Sn/10-PbTe sample displays a concave function of $\mu_0 H_c(T)$ (Fig. 2b), which can be fitted by a formula designated for the two-band situation[26] (see Methods). In contrast to the behaviours of samples in regime II, we observe no deviation from a single-band superconductor for samples in regime I to the lowest attainable temperature. Furthermore, they show different activated behaviours in the presence of a magnetic field. For 3-Sn/8-PbTe, fittings to the activated region extrapolate to a fixed point: $1/T_c$. In contrast, 3-Sn/10-PbTe displays a continuous shift of the crossing between the adjacent extrapolated lines (dashed in Fig. 2d). The distinction is better captured by the extracted activation energy U_H and the intercept of the fitting $\ln R_0(\mu_0 H)$. In regime I, U_H scales linearly with $\ln(\mu_0 H)$, which can be described by the collective creeping of vortices[4], and the slope yields a London penetration depth Λ of 700 nm (see Methods). The Ginzburg–Landau parameter $\kappa = \Lambda/\xi$ is therefore about 23, which is much larger than $1/\sqrt{2}$, as expected for a type II superconductor. In regime II, we obtain instead a convex dependence of both U_H on $\ln(\mu_0 H)$ (Fig. 2e) and $\ln R_0$ on $U_H/k_B T_c$ (Fig. 2f). This nonlinearity may stem from field-dependent superconducting parameters of d_{sc} and Λ for multiband superconductors[28,29].

The transition from a single-band to a two-band system is corroborated by ARPES. Figure 3a displays the data of a trilayer stanene with increasing N_{PbTe}. Two valence bands can be identified: a parabolic band with its highest intensity (dark colour) below the Fermi level (E_F) and a linearly-dispersed band (white) with its two arms crossing E_F. The position of the Fermi level is distinctly different from that of bulk α-Sn (refs [30,31]). Superconductivity in few-layer stanene here may therefore stem from the enhanced density of states. By increasing N_{PbTe}, the two valence bands sink, evidenced by the decrease in energy (Fig. 3b) of the parabolic band as well as the shrinking Fermi momentum for the linear band (Fig. 3c). This indicates an increase of electron transfer from PbTe. Concomitantly, a third band becomes discernible at the Fermi level. We focus on the region just below the Fermi level in the momentum range of $[-0.2, 0.2]$ Å^{-1}. The overall shape evolves from a rounded pyramid for 3-Sn/6-PbTe to an hour-glass structure for $N_{PbTe} \geq 10$. Such an evolution is in direct contrast to the monotonic behaviour of the residual photoelectron intensities in the gapped region, as seen in $SrTiO_3$ due to correlation effects[32]. We therefore attribute the hour-glass feature to the emergence of an electron pocket around the Γ point. In the case of 3-Sn/6-PbTe, this electron pocket may just touch the Fermi level, providing negligible contribution to transport. With further doping, the central electron pocket is significantly enlarged while the outer linear band shrinks. The trilayer stanene on PbTe with $N_{PbTe} \geq 10$ therefore behaves as a two-band superconductor. At higher doping, the enhanced interband scattering may suppress superconductivity[33], thus explaining the drop of T_c for 3-Sn on 20-PbTe (Fig. 1c,e). In addition, we estimate electron–phonon coupling constant to be 0.5 ± 0.2 for the hole band[34],

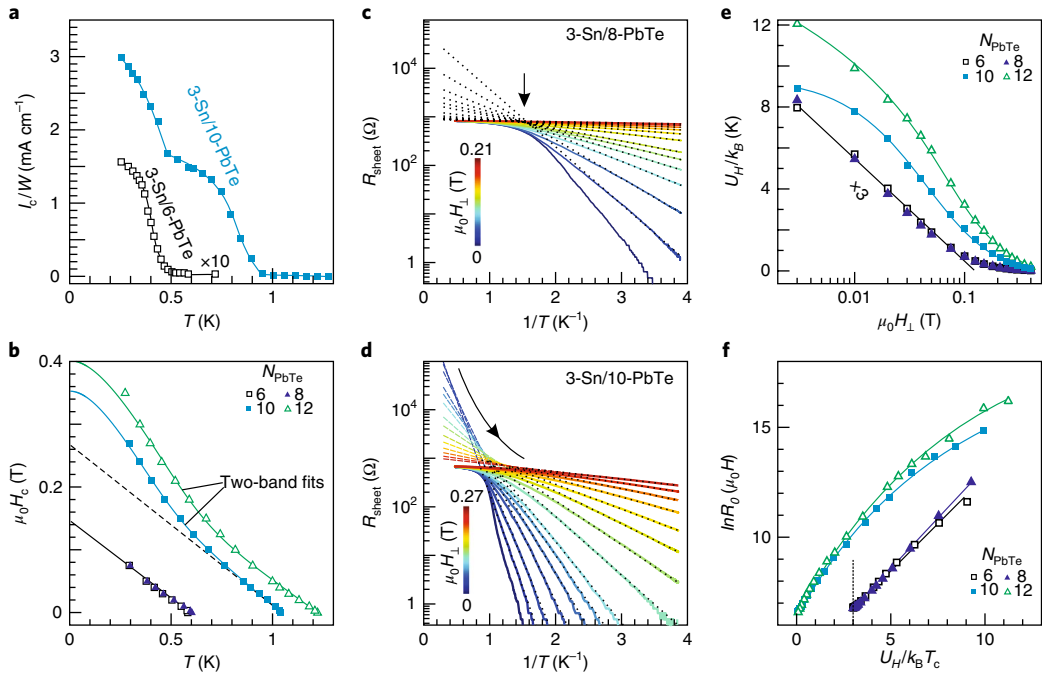

Fig. 2 | Single-band to two-band transition of a trilayer stanene. a, Critical current normalized by width of sample. Curves are guides to the eye. **b**, Upper critical field as a function of temperature. From the two-band fitting, we obtain the ratio between the diffusivities of the two bands: $D_2/D_1 \sim 0.3$. The fitting also yields the electron–phonon coupling constants for the two respective bands and the interband one: $\lambda_{11} = 0.28$, $\lambda_{22} = 0.26$, $\lambda_{12} = 0.013$ (see Methods). **c**,**d**, Arrhenius plots of the sheet resistance at different magnetic fields for two 3-Sn samples with different numbers of PbTe layers. Dotted lines are linear fits to the data in the low-temperature regime, reflecting the thermal activation behaviour. **e**, Activation energy U_H/k_B as a function of the perpendicular magnetic field. **f**, Extracted intercepts from fitting the activated transport (dotted lines in **c** and **d**). Data points for $N_{PbTe} = 6$ and 8 are horizontally offset for clarity (the dotted line marks the zero point).

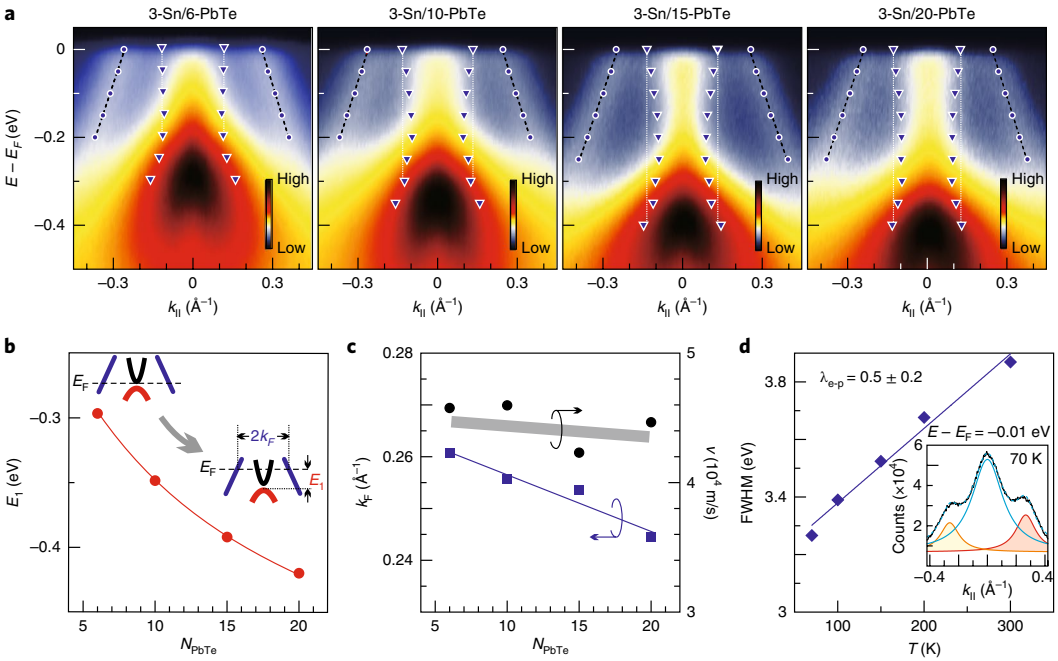

Fig. 3 | ARPES studies of a trilayer stanene. a, Band structure around the Γ point for 3-Sn grown on increasing numbers of PbTe layers. Circles mark the linear dispersion of the hole bands, with dashed lines as linear fits. Triangles demarcate the width of the central peak around $k_{||} = 0$ at different energies. Dotted vertical lines are guides to the eye. **b**, Downward shift of the energy band. The inset explains the definitions of E_1 and k_F. **c**, Fermi momentum (k_F) and the velocity of the linearly dispersed hole band as a function of N_{PbTe}. **d**, Energy width of the hole band as a function of temperature for a 3-Sn/10-PbTe sample. The electron–phonon coupling constant is estimated from a linear fitting (solid line) to the data points[34]. The estimated electron–phonon coupling constant is 0.5 ± 0.2 with the uncertainty obtained by taking into account both the Lorentzian and the linear fittings involved (see Extended Data Figure 4). The inset illustrates the Lorentzian fitting to the momentum distribution curve at $E - E_F = -0.01$ eV, 70 K. The shaded peaks reflect the hole bands. The energy width is calculated from the product of the momentum width of the shaded peaks (Δk) and the slope of the band (dE/dk).

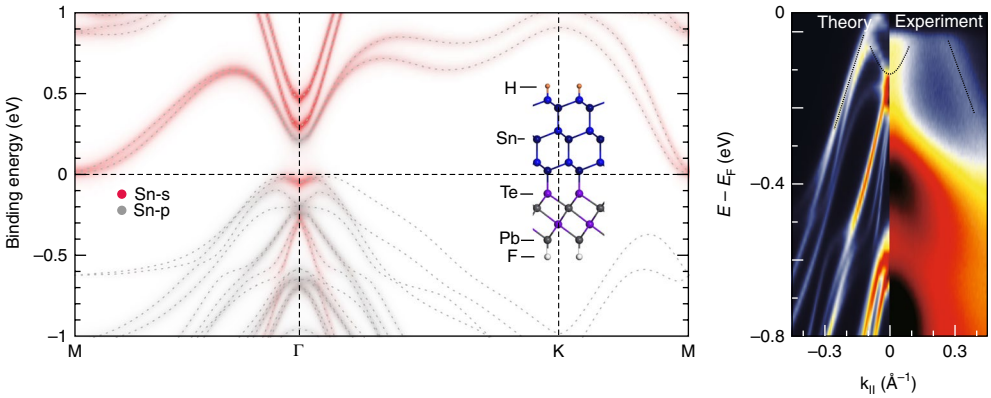

Fig. 4 | Calculated band structure of a trilayer stanene on PbTe. The inset illustrates the atomic model considered in the first-principles calculation. A hydrogenated trilayer stanene is placed on top of the PbTe substrate, which is simulated by a slab of two PbTe layers saturated by fluorine on the bottom. Red (grey) colour highlights the contributions from Sn s (p) orbitals, obtained by projecting the Bloch wavefunction onto the corresponding orbitals. This indicates an s–p band inversion at the Γ point. The right-hand panel compares the calculated bands with the ARPES data from 3-Sn/15-PbTe.

which agrees with our transport result by fitting the upper critical field data (Fig. 2b). In comparison, for the bulk β-Sn $\lambda \sim 0.7$ (ref. [11]).

We also performed first-principles calculations for a trilayer stanene grown on PbTe (see Methods). The calculated band structure, displayed in Fig. 4, looks somewhat complicated, since orbitals of stanene and PbTe hybridize strongly with each other, showing significant Rashba splitting. Nevertheless, there exist two series of valence bands mainly contributed by stanene located about 0–0.6 eV below the valence band maximum. Importantly, the top valence bands are "M" shaped, which could introduce an "electron pocket" centred at Γ if E_F is placed slightly below the valence band maximum. These features echo the ARPES data. Furthermore, orbital analysis shows that Sn s (p) orbitals make a significant contribution to the lowest conduction (highest valence) band, except at Γ, where an s–p band inversion happens. This band inversion results in a topologically non-trivial phase[16,20,35]. The trilayer stanene grown on PbTe is therefore a 2D topological insulator with $Z_2 = 1$ in theory (see Extended Data Figure 5). We note that a band inversion may be induced in $Pb_{1-x}Sn_xTe$ alloy by increasing Sn, which is accompanied by reopening of the bulk band gap[24,36,37]. Experimentally, we observed no bulk band gap closing in PbTe with the low-temperature deposition of Sn[19], ruling out a possible topological transition in the PbTe substrate.

The delicate dependence of T_c on N_{Sn} can be employed for an in-plane integration of topological insulator and superconductor in the same material with tunable properties. Another direction for future endeavour is to investigate the proximity effect in the vertical direction. Our sandwich structure allows atomically sharp interfaces between a superconductor, a tunable barrier and a topological insulator—Bi_2Te_3. The Fermi momentum of few-layer stanene is comparable to that of Bi_2Te_3. Furthermore, the superconducting thickness we estimated can be larger than the total thickness of Sn and PbTe layers (Extended Data Figure 3d), such that Cooper pairs may travel into Bi_2Te_3. In addition, stanene is robust against air exposure and can protect the more sensitive Bi_2Te_3. In general, the observation of superconductivity in few-layer stanene enriches the material pool for constructing topological devices.

Methods

Methods, including statements of data availability and any associated accession codes and references, are available at https://doi.org/10.1038/s41567-017-0031-6.

Received: 19 July 2017; Accepted: 4 December 2017;
Published online: 15 January 2018

References

1. Saito, Y., Nojima, T. & Iwasa, Y. Highly crystalline 2D superconductors. *Nat. Rev. Mater.* **2**, 16094 (2017).
2. Brun, C., Cren, T. & Roditchev, D. Review of 2D superconductivity: the ultimate case of epitaxial monolayers. *Supercond. Sci. Technol.* **30**, 013003 (2017).
3. Xing, Y. et al. Quantum Griffiths singularity of superconductor–metal transition in Ga thin films. *Science* **350**, 542–545 (2015).
4. Saito, Y., Kasahara, Y., Ye, J., Iwasa, Y. & Nojima, T. Metallic ground state in an ion gated two-dimensional superconductor. *Science* **350**, 409–413 (2015).
5. Tsen, A. W. et al. Nature of the quantum metal in a two-dimensional crystalline superconductor. *Nat. Phys.* **12**, 208–212 (2016).
6. Lu, J. M. et al. Evidence for two-dimensional Ising superconductivity in gated MoS_2. *Science* **350**, 1353–1357 (2015).
7. Xi, X. et al. Ising pairing in superconducting $NbSe_2$ atomic layers. *Nat. Phys.* **12**, 139–143 (2016).
8. Qin, S., Kim, J., Niu, Q. & Shih, C.-K. Superconductivity at the two-dimensional limit. *Science* **324**, 1314–1317 (2009).
9. Zhang, T. et al. Superconductivity in one-atomic-layer metal films grown on Si(111). *Nat. Phys.* **6**, 104–108 (2010).
10. Meissner, W. & Ochsenfeld, R. Ein neuer Effekt bei Eintritt der Supraleitfähigkeit. *Naturwissenschaften* **21**, 787–788 (1933).
11. Chang, K. J. & Cohen, M. L. Electron–phonon interactions and superconductivity in Si, Ge, and Sn. *Phys. Rev. B* **34**, 4552–4557 (1986).
12. Wang, L. L. et al. Epitaxial growth and quantum well states study of Sn thin films on Sn induced Si(111)-$2\sqrt{3} \times 2\sqrt{3}$ R30° V. *Phys. Rev. B* **77**, 205410 (2008).
13. Molle, A. et al. Buckled two-dimensional Xene sheets. *Nat. Mater.* **16**, 163–169 (2017).
14. Xu, Y., Gan, Z. & Zhang, S.-C. Enhanced thermoelectric performance and anomalous Seebeck effects in topological insulators. *Phys. Rev. Lett.* **112**, 226801 (2014).
15. Wang, J., Xu, Y. & Zhang, S.-C. Two-dimensional time-reversal-invariant topological superconductivity in a doped quantum spin-Hall insulator. *Phys. Rev. B* **90**, 054503 (2014).
16. Xu, Y. et al. Large-gap quantum spin Hall insulators in tin films. *Phys. Rev. Lett.* **111**, 136804 (2013).
17. Wu, S.-C., Shan, G. & Yan, B. Prediction of near-room-temperature quantum anomalous Hall effect on honeycomb materials. *Phys. Rev. Lett.* **113**, 256401 (2014).
18. Zhu, F.-F. et al. Epitaxial growth of two-dimensional stanene. *Nat. Mater.* **14**, 1020–1025 (2015).
19. Y. Zang, et al. Realizing an epitaxial stanene with an insulating bandgap. Preprint at http://arXiv.org/abs/1711.07035.
20. Chou, B.-H. et al. Hydrogenated ultra-thin tin films predicted as two-dimensional topological insulators. *New J. Phys.* **16**, 115008 (2014).
21. Chang, W. et al. Hard gap in epitaxial semiconductor–superconductor nanowires. *Nat. Nanotechnol.* **10**, 232–236 (2015).
22. Van de Walle, C. G. Hydrogen as a cause of doping in zinc oxide. *Phys. Rev. Lett.* **85**, 1012–1015 (2000).
23. Chang, K. et al. Discovery of robust in-plane ferroelectricity in atomic-thick SnTe. *Science* **353**, 274–278 (2016).

24. Yan, C. et al. Experimental observation of Dirac-like surface states and topological phase transition in $Pb_{1-x}Sn_xTe(111)$ films. *Phys. Rev. Lett.* **112**, 186801 (2014).
25. Talantsev, E. F. et al. On the origin of critical temperature enhancement in atomically thin superconductors. *2D Mater.* **4**, 025072 (2017).
26. Gurevich, A. Limits of the upper critical field in dirty two-gap superconductors. *Physica C* **456**, 160–169 (2007).
27. Weng, Z. F. et al. Two-gap superconductivity in $LaNiGa_2$ with nonunitary triplet pairing and even parity gap symmetry. *Phys. Rev. Lett.* **117**, 027001 (2016).
28. Zehetmayer, M. A review of two-band superconductivity: materials and effects on the thermodynamic and reversible mixed-state properties. *Supercond. Sci. Technol.* **26**, 043001 (2013).
29. Civale, L. & Serquis, A. *MgB2 Superconducting Wires Ch. 1* (World Scientific, Singapore, 2016).
30. Barfuss, A. et al. Elemental topological insulator with tunable Fermi level: strained α-Sn on InSb(001). *Phys. Rev. Lett.* **111**, 157205 (2013).
31. Rojas-Sanchez, J.-C. et al. Spin to charge conversion at room temperature by spin pumping into a new type of topological insulator: α-Sn films. *Phys. Rev. Lett.* **116**, 096602 (2016).
32. Meevasana, W. et al. Creation and control of a two-dimensional electron liquid at the bare $SrTiO_3$ surface. *Nat. Mater.* **10**, 114–118 (2011).
33. Boschker, H., Richter, C., Fillis-Tsirakis, E., Schneider, C. W. & Mannhart, J. Electron–phonon coupling and the superconducting phase diagram of the $LaAlO_3$–$SrTiO_3$ interface. *Sci. Rep.* **5**, 12309 (2015).
34. Matetskiy, A. V. et al. Two-dimensional superconductor with a giant Rashba effect: one-atom-layer Tl–Pb compound on Si(111). *Phys. Rev. Lett.* **115**, 147003 (2015).
35. Xu, Y., Tang, P. & Zhang, S.-C. Large-gap quantum spin Hall states in decorated stanene grown on a substrate. *Phys. Rev. B* **92**, 081112(R) (2015).
36. Dimmock, J. O., Melngailis, I. & Strauss, A. J. Band structure and laser action in $Pb_xSn_{1-x}Te$. *Phys. Rev. Lett.* **16**, 1193–1196 (1966).
37. Arachchige, I. U. & Kanatzidis, M. G. Anomalous band gap evolution from band inversion in $Pb_{1-x}Sn_xTe$ nanocrystals. *Nano Lett.* **9**, 1583–1587 (2009).

Acknowledgements

We thank Hong Yao and Canli Song for useful discussions. This work is financially supported by the Ministry of Science and Technology of China (2017YFA0304600, 2017YFA0302902), the National Natural Science Foundation of China (grant no. 11604176) and the Beijing Advanced Innovation Center for Future Chip (ICFC). Y.X. acknowledges support from Tsinghua University Initiative Scientific Research Program and the National Thousand-Young-Talents Program. S.-C.Z. is supported by the US Department of Energy, Office of Basic Energy Sciences, Division of Materials Sciences and Engineering under contract no. DE-AC02-76SF00515.

Author contributions

M.L. and Y.Z. contributed equally to this work. D.Z., K.H. and Q.-K.X. conceived the project. Y.Z. grew the samples and carried out ARPES measurements with the assistance of Y.G., M.L. and D.Z. carried out the transport measurements with the assistance of K.Z., M.L., D.Z., H.L., X.-P.H. and Y.-Y.W. made the two-coil mutual inductance measurements. Z.G. and Y.X. carried out first-principles calculations. D.Z. and Y.X. analysed the data and wrote the paper with input from K.H., X.-C.M., S.-C.Z. and Q.-K.X. All authors discussed the results and commented on the manuscript.

Competing interests

The authors declare no competing financial interests.

Additional information

Supplementary information is available for this paper at https://doi.org/10.1038/s41567-017-0031-6.

Reprints and permissions information is available at www.nature.com/reprints.

Correspondence and requests for materials should be addressed to D.Z. or Y.X. or Q.-K.X.

Publisher's note: Springer Nature remains neutral with regard to jurisdictional claims in published maps and institutional affiliations.

Methods

Growth. We use molecular beam epitaxy to grow our heterostructures (Omicron, base pressure 1×10^{-10} mbar). To ensure lattice matching, five quintuple layers of Bi_2Te_3 were first grown on top of Si(111) substrates. This was followed by the layer-by-layer growth of PbTe. Finally, we deposited Sn at a substrate temperature of around 120 K. The sample is then annealed at temperatures up to 400 K to improve the film quality. The crystalline quality is monitored by in situ reflective high-energy electron diffraction and scanning tunnelling microscopy (see Extended Data Figure 6). A layer-by-layer growth is maintained from a monolayer up to the quintuple layer. Above five layers, the growth tends to form islands. The lattice constant of stanene expands as the number of PbTe layers increases, as revealed by reflective high-energy electron diffraction[19].

Transport. Samples grown on intrinsic Si(111) substrate were employed for low-temperature transport measurements in a closed-cycle system (Oxford Instruments TelatronPT) equipped with an He-3 insert (base temperature = 0.25 K). The temperature sensor was placed directly below the sample stage and positioned in an orientation with minimal magnetoresistances. Freshly cut indium cubes were cold pressed onto the sample as contacts. Standard lock-in techniques were employed to determine the sample resistance in a four-terminal configuration with a typical excitation current of 100 nA at 13 Hz.

To fit upper critical field as a function of temperature in the two-band regime, we employ the formula[26]

$$\ln\frac{T}{T_c} = -\frac{\left[U\left(\frac{eD_1\mu_0H_{c2}}{hT}\right)+U\left(\frac{eD_2\mu_0H_{c2}}{hT}\right)+\frac{\sqrt{(\lambda_{11}-\lambda_{22})^2+4\lambda_{12}^2}}{\lambda_{11}\lambda_{22}-\lambda_{12}^2}\right]}{2}+$$
$$\left[\frac{\left(U\left(\frac{eD_1\mu_0H_{c2}}{hT}\right)-U\left(\frac{eD_2\mu_0H_{c2}}{hT}\right)-\frac{\lambda_{11}-\lambda_{22}}{\lambda_{11}\lambda_{22}-\lambda_{12}^2}\right)^2}{4}+\frac{\lambda_{12}^2}{(\lambda_{11}\lambda_{22}-\lambda_{12}^2)^2}\right]^{\frac{1}{2}},$$

where $U(x)=\psi\left(\frac{1}{2}+x\right)-\psi\left(\frac{1}{2}\right)$, with ψ the digamma function. D_1 and D_2 reflect the diffusivities of the two bands. λ_{11}, λ_{22} and λ_{12} are intraband and interband electron–phonon coupling constants, respectively. We fit the data of 3-Sn/10-PbTe with D_1, D_2, λ_{11}, λ_{22} and λ_{12} as fitting parameters. We then use the extracted values of λ_{11}, λ_{22} and λ_{12} and fit the data of 3-Sn/12-PbTe with D_1 and D_2 as free parameters.

For the activated transport, we use $R_{\mathrm{sheet}}=R_0(\mu_0H)e^{-\frac{U_H}{T}}$ to fit the data. U_H represents the activation energy. In regime I, $R_0(\mu_0H)$ scales as $R_0e^{\frac{U_H}{T_c}}$, with R_0 being independent of μ_0H. Also, U_H scales linearly with $\ln(\mu_0H)$ such that $-\frac{dU_H}{d\ln\mu_0H}=\frac{\Phi_0^2d}{256\pi^3\Lambda^2}$ (ref. [38]). Here Φ_0 is the flux quantum and Λ the London penetration depth normal to the superconducting film.

ARPES. Samples grown on highly doped Si(111) substrates were transferred to the analysis chamber without breaking the ultrahigh vacuum. ARPES with a photon energy of 21.22 eV (He-I light) was carried out with a Scienta R4000 spectrometer. For a quantitative analysis, we first extract the momentum k at a series of binding energies by fitting the peaks in the corresponding momentum distribution curves with Lorentzian functions. The obtained data points $k(E)$ (white circles in Fig. 3a) are then linearly fitted (dashed lines) to extract dE/dk as well as k_F.

First-principles calculations. Density functional theory calculations were performed with the Vienna ab initio simulation package, using the projector-augmented-wave potential, the Perdew–Burke–Ernzerhof exchange–correlation functional and the plane-wave basis with an energy cut-off of 400 eV. The periodic slab approach was employed to model stanene grown on PbTe, using a vacuum layer of 12 Å and a $12\times12\times1$ Monkhorst–Pack k grid. A slab of two Pb–Te bilayers with a surface lattice constant of 4.568 Å (based on the experimental value of bulk) was used to simulate the substrate, in which the bottom Pb–Te bilayer was fixed during relaxation and the bottom Pb atoms were saturated by fluorine to remove the dangling bonds on the bottom. The spin–orbit coupling was included in the self-consistent calculations of electronic structure.

Data availability. The data that support the findings of this study are available from the authors upon reasonable request.

References

38. Ephron, D., Yazdani, A., Kapitulnik, A. & Beasley, M. R. Observation of quantum dissipation in the vortex state of a highly disordered superconducting thin film. *Phys. Rev. Lett.* **76**, 1529–1532 (1996).